Electronic Supplementary Information (ESI) for

Ultrafast ring-opening and solvent dependent product relaxation of photochromic spironaphthopyran

Simon F. Bittmann, Raison Dsouza, Khalid M. Siddiqui, Stuart A. Hayes, Andreas Rossos, Gastón Corthey, Michał Kochman, Valentyn I. Prokhorenko, R. Scott Murphy, Heinrich Schwoerer and R. J. Dwayne Miller.

correspondence to: dwayne.miller@mpsd.mpg.de

Contents

1 Electronic structure calculations **2**

2 Excited state dynamics simulations **7**
2.1 Computational details and example trajectories 7
2.2 Population modeling 10
2.3 Trajectory analysis 10

3 Steady-state absorption measurements **12**

4 Transient absorption spectroscopy **15**
4.1 UV/Vis transient absorption maps 15
4.2 UV/Vis transient absorption maps-False Colour 16
4.3 Integrated TA product bands 16
4.4 UV/UV transient absorption maps 17
4.5 Fluence dependence 18
4.6 Acquisition scheme 18

5 Global analyses **21**

6 Gaussian modeling **24**
6.1 Model comparison 24
6.2 Relaxation dynamics analysis 27

7 Centre of gravity analysis **29**

References **30**

1 Electronic structure calculations

All calculations involving electronic ground and excited state energies were performed using the Gaussian program suite[1]. The electronic ground state energies and frequencies were calculated at the level of Density Functional Theory (DFT) using CAM-B3LYP[2] functional and def2SVP basis set. CAM-B3LYP developed by Handy and coworkers adds the long-range (asymptotic) correction term to the existing exchange-correlation functional B3LYP. This functional is perfectly suited for large poly-atomic molecules such as spironaphthopyran due to the presence of charge-transfer-like excited state character between two interacting moieties. The structure of the ground-state conformer is tabulated in Table S3.

The electronic excited states of SNP are calculated using Linear Response Time-dependent Density Functional Theory (LR-TDDFT) with the same functional and basis set. The excited state energies and oscillator strengths are shown in Table S1. The conformer corresponding to the excited state singlet (S1) minimum is also given below S4. Recent work on excited state dynamics[3] using higher correlated methods such as ADC(2) motivated us to perform it on SNP in order to compare with TDDFT. Furthermore, ADC(2) provides deeper insight into the Electronic Structure (see Table S2). To compare with experiments, the photo-absorption was simulated using the conformers generated from a Wigner Distribution of the ground state normal modes (see Figure S1). For each conformer, several single-point TDDFT and ADC(2) calculations were performed. Analytically obtained gradients were used for Molecular Dynamics. All ADC(2) and MP2 calculations were performed using the Turbomole package[4].

Table S1: Electronic Excited State energies and oscillator strengths f using LR-TDDFT/CAM-B3LYP/def2SVP.

Electronic Excited State Energies		
Energy Ordering	TDDFT (eV)	f
1	4.1415	0.1611
2	4.5318	0.0738
3	4.6543	0.0273
4	5.0514	0.0665
5	5.2018	0.0393
6	5.7107	0.4317
7	5.7873	0.2713
8	6.0303	0.1024
9	6.0806	1.2314
10	6.1995	0.0070

Table S2: Electronic Excited State energies and oscillator strengths f using ADC(2)/cc-pVDZ.

Electronic Excited State Energies		
Energy Ordering	ADC(2) (eV)	f
1	3.74473	0.08163735
2	4.19060	0.00978647
3	4.41480	0.04822508
4	4.70426	0.05783651
5	4.87489	0.00341588
6	5.30625	0.82971973
7	5.48287	0.21979856
8	5.58325	0.44410381
9	5.68407	0.03780126
10	5.84517	0.06521965

Table S3: Optimized Electronic Ground State Configuration DFT/CAM-B3LYP.

C	-1.04661	-0.70260	0.04805
C	-1.55086	-1.99844	-0.21807
C	-2.89870	-2.19084	-0.33444
C	-3.81290	-1.11075	-0.19028
C	-5.21167	-1.30693	-0.31666
C	-6.08909	-0.26200	-0.17493
C	-5.59328	1.03141	0.10021
C	-4.24354	1.25208	0.22790
C	-3.30780	0.19248	0.08851
C	-1.89225	0.38040	0.21430
C	-1.25806	1.64675	0.55416
C	0.07272	1.76962	0.60778
C	1.01132	0.64611	0.27917
C	3.14601	-0.11377	0.72406
C	4.20155	-0.77347	1.34285
C	5.24294	-1.24867	0.53759
C	5.22405	-1.07781	-0.84208
C	4.14905	-0.41488	-1.45074
C	3.11774	0.06222	-0.66549
C	1.87488	0.85340	-1.02516
C	1.61343	0.10707	2.64552
C	2.25980	2.33157	-1.19527
C	1.15319	0.35947	-2.27523
N	2.01144	0.45047	1.30393
O	0.29265	-0.60337	0.14866
H	-0.83617	-2.81530	-0.32690
H	-3.29318	-3.18765	-0.54496
H	-5.57929	-2.31357	-0.53069
H	-7.16406	-0.42470	-0.27443
H	-6.29010	1.86516	0.21097
H	-3.89039	2.26240	0.43498
H	-1.88021	2.50869	0.79738
H	0.53921	2.71084	0.89786
H	4.22156	-0.92702	2.42249
H	6.08029	-1.77139	1.00577
H	6.04286	-1.46376	-1.45214
H	4.12967	-0.28260	-2.53553
H	1.40143	-0.97142	2.76302
H	2.40304	0.38634	3.35882
H	0.70797	0.66846	2.91197
H	2.73402	2.73005	-0.28699
H	2.98124	2.42811	-2.01902
H	1.38287	2.95072	-1.43643
H	0.19692	0.88815	-2.41020
H	0.95200	-0.71740	-2.22660
H	1.76764	0.55554	-3.16654

Table S4: Optimized Electronic Excited State (S1) Configuration TDDFT/CAM-B3LYP.

C	-0.97802	-0.73783	0.19051
C	-1.45289	-2.01055	-0.12939
C	-2.81384	-2.19755	-0.34203
C	-3.72995	-1.11321	-0.28819
C	-5.10663	-1.29680	-0.52164
C	-6.00067	-0.22880	-0.49089
C	-5.54433	1.06360	-0.22895
C	-4.18533	1.27349	0.01404
C	-3.25800	0.21753	0.00651
C	-1.85825	0.40962	0.28860
C	-1.26758	1.63020	0.70458
C	0.08936	1.75856	0.87338
C	1.01574	0.67280	0.50508
C	3.17894	-0.10100	0.72454
C	4.28705	-0.75339	1.25066
C	5.22571	-1.27963	0.35567
C	5.05513	-1.16450	-1.01934
C	3.92934	-0.50625	-1.53340
C	2.99981	0.02260	-0.65854
C	1.74331	0.82858	-0.91864
C	1.88387	0.23391	2.80168
C	2.12664	2.29973	-1.13683
C	0.89807	0.33003	-2.08169
N	2.12062	0.50105	1.40410
O	0.31843	-0.61883	0.45735
H	-0.73760	-2.83149	-0.18373
H	-3.19760	-3.19465	-0.56791
H	-5.47170	-2.30470	-0.73276
H	-7.06167	-0.40826	-0.67834
H	-6.23816	1.90547	-0.21667
H	-3.83911	2.28952	0.20716
H	-1.90647	2.48680	0.92178
H	0.53385	2.68842	1.22683
H	4.42366	-0.86442	2.32695
H	6.10241	-1.79882	0.74967
H	5.79517	-1.59011	-1.69957
H	3.79205	-0.41585	-2.61378
H	1.71504	-0.83983	3.00234
H	2.73997	0.57131	3.40468
H	0.99737	0.79468	3.12609
H	2.68304	2.69874	-0.27723
H	2.77286	2.37891	-2.02323
H	1.23377	2.92093	-1.29773
H	-0.06396	0.86263	-2.12772
H	0.69998	-0.74699	-2.01802
H	1.42386	0.52346	-3.02881

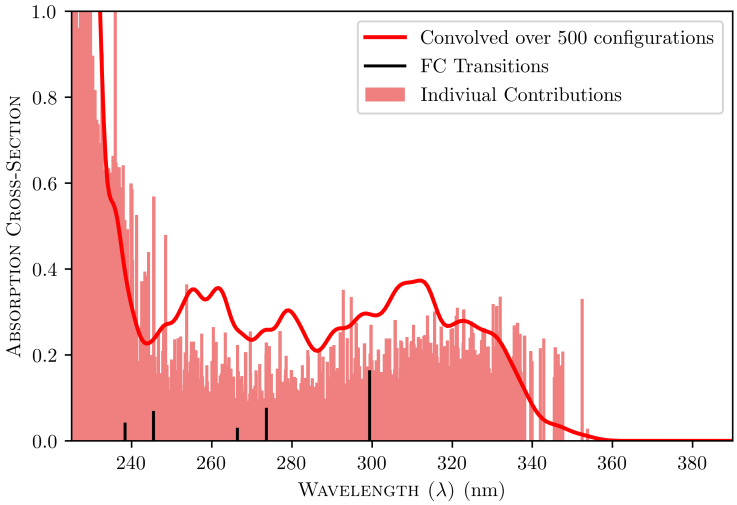

(a) Calculated using TDDFT

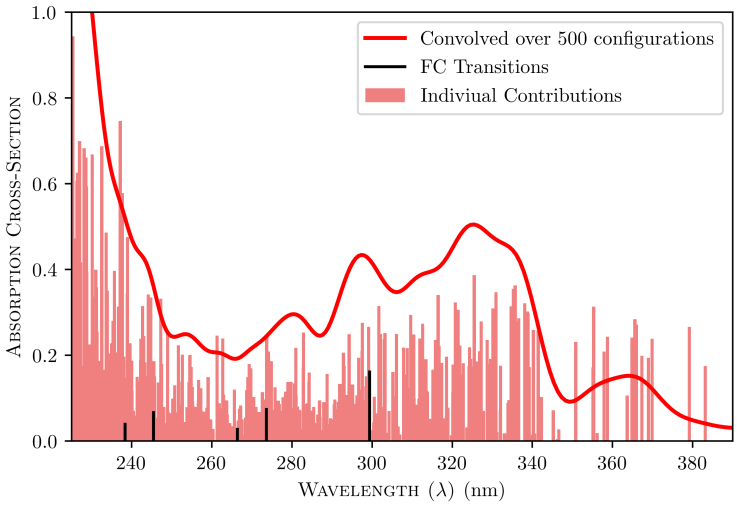

(b) Calculated using ADC(2)

Fig. S1: Photo-Absorption Spectra calculated from various configurations generated by Wigner sampling of Ground State Normal Modes.

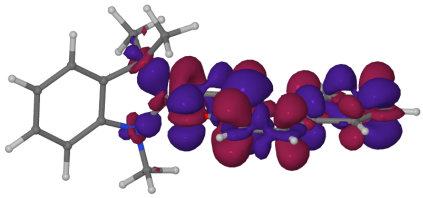

(a) Between First Singlet Excited State (S1) and Ground state

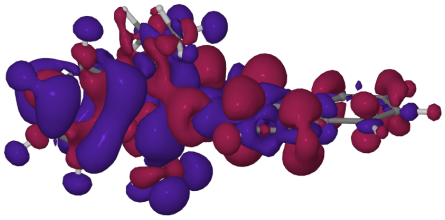

(b) Between Second Singlet Excited State (S2) and Ground state

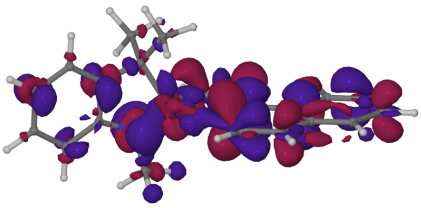

(c) Between Third Singlet Excited State (S3) and Ground state

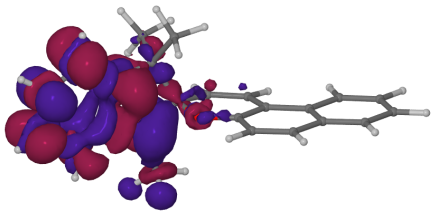

(d) Between Fourth Singlet Excited State (S4) and Ground state

Fig. S2: The electron density difference maps between the ground state and the first four singlet excited states, calculated at TDDFT level.

2 Excited state dynamics simulations

2.1 Computational details and example trajectories

The entire molecule was treated at TDDFT level using analytically obtained gradients for molecular dynamics propagation. The molecule was allowed to propagate at a given time in only one potential energy surface. Transitions of the molecules between the electronic states were modelled using a threshold value for the energy gap. The two reaction pathways as obtained from the Surface-Hopping simulations are analyzed here. For demonstrative purposes, one trajectory from each pathway is further characterized using bond distances and dihedral angles. All observables and conclusions about a certain pathway are done by averaging over all respective simulated trajectories.

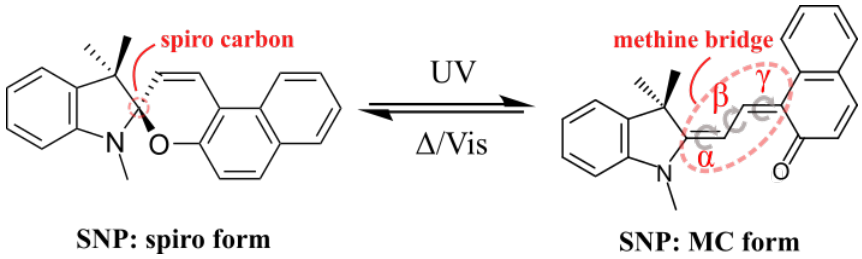

(a)

Fig. S3: Reaction Scheme.

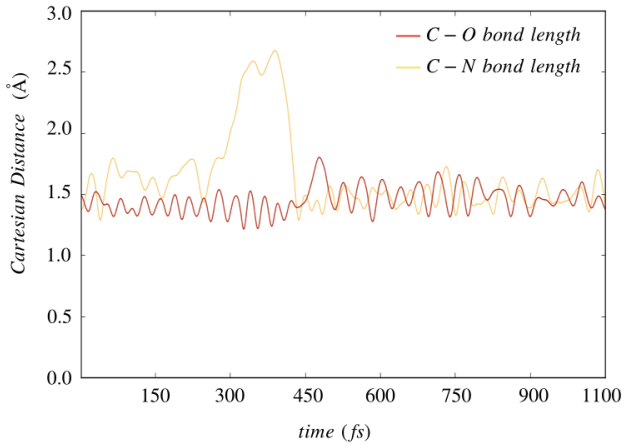

Fig. S4: Representative trajectory which passes via non-radiative decay from S1 to the ground state SNP: Bond distances.

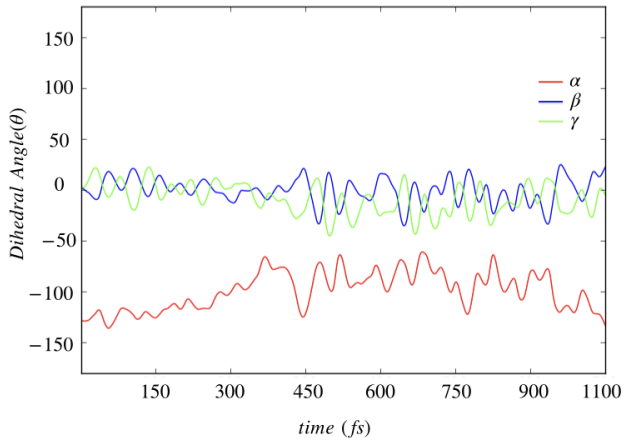

Fig. S5: Representative trajectory which passes via non-radiative decay from S1 to the ground state SNP: Dihedral angles along the methine bridge.

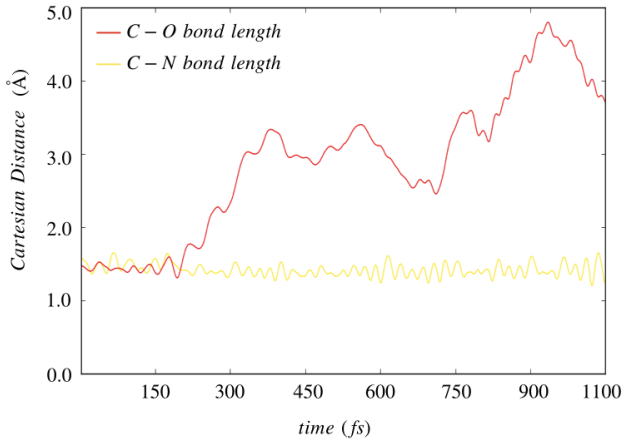

Fig. S6: Representative trajectory leading via non-radiative decay and bond breaking to Merocyanine: Bond distances.

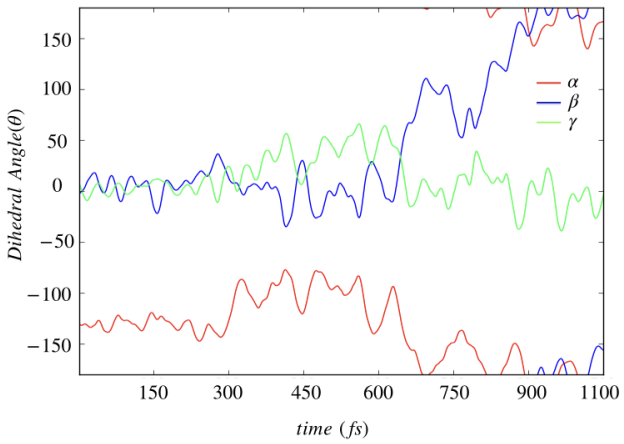

Fig. S7: Representative trajectory leading via non-radiative decay and bond breaking to Merocyanine: Dihedral angles along the methine bridge.

2.2 Population modeling

In the simulations, S_3 and S_2 were initially equally populated and close in energy. A combined kinetic fit of all four participating states was hence impeded, as population transfer from S_2 back to S_3 was not inhibited. Instead, the two states were treated as a superposition state to obtain an effective internal conversion rate k_{n1} from higher lying excited states to the S_1 state. This results in the kinetic model given in the main text:

$$S_n \xrightarrow{k_{n1}} S_1 \xrightarrow{k_{10}} S_0 \tag{S2.2.1}$$

with the rate constants k_{ij} for the population transfer from S_i to S_j. The resulting rate equations are (brackets indicate populations as a function of time t):

$$\frac{\mathrm{d}[S_n]}{\mathrm{d}t} = -k_{n1}[S_n], \tag{S2.2.2}$$

$$\frac{\mathrm{d}[S_1]}{\mathrm{d}t} = k_{n1}[S_n] - k_{10}[S_1] \tag{S2.2.3}$$

and

$$\frac{\mathrm{d}[S_0]}{\mathrm{d}t} = k_{10}[S_1]. \tag{S2.2.4}$$

By solving the differential equations S2.2.2 and S2.2.3, making use of the fact that the total population is constant, the populations as a function of time are obtained:

$$[S_n] = [S_n]_0 \cdot e^{-k_{n1}t}, \tag{S2.2.5}$$

$$[S_1] = \frac{k_{n1}[S_n]_0}{k_{10} - k_{n1}} \left(e^{-k_{n1}t} - e^{-k_{10}t}\right) + [S_1]_0 \cdot e^{-k_{10}t}, \tag{S2.2.6}$$

$$[S_0] = [S_n]_0 + [S_1]_0 + [S_0]_0 - [S_n] - [S_1]. \tag{S2.2.7}$$

where $[S_i]_0$ is the initial population of state S_i at $t = 0$. Given by the initial conditions of the simulations, $[S_1]_0$ and $[S_0]_0$ are equal to zero and $[S_n]_0$ equal to one.
The results of this fit were $k_{n1} = 1.13 \cdot 10^{13}\,\mathrm{s}^{-1}$ and $k_{10} = 7.93 \cdot 10^{11}\,\mathrm{s}^{-1}$ corresponding to time constants of 88.4 fs and 1.26 ps, respectively.

2.3 Trajectory analysis

In this section, a more detailed analysis of the obtained trajectories is given, distinguishing between those that result in an open-ring form and those that lead back to the initial form. As mentioned in the main manuscript, a time constant for the bond breaking is obtained by fitting the population of bond-broken species with an exponential function (see Fig S8 a). The point of bond breaking was defined by setting a threshold value for the C-O bond elongation, in the shown case 1 Å. The time constant of around 350 fs stated in the manuscript was extracted by averaging over the time constants that did not show a significant dependence of the threshold value, i.e. between 0.4 and 1.2 Å(see Fig S8 b). The fits were started from 90 fs, the previously obtained transfer rate to the S_1 state, which gave a better representation of the trajectories than starting from t = 0 fs. Furthermore, it was observed by examining the trajectories that ring-opening only happened in S_1.

Fig S9 demonstrates how the correlation between S1 to S0 hopping and an elongation of the C_{spiro}-N bond in the internal conversion trajectories leading back to the spiro-form was characterised. A threshold for the elongation was defined by taking the half maximum value. The time of elongation was then obtained by taking the mean value of all time points at which the C-N bond exceeded this threshold, while the S1 to S0 hopping time was directly obtained from the simulations.

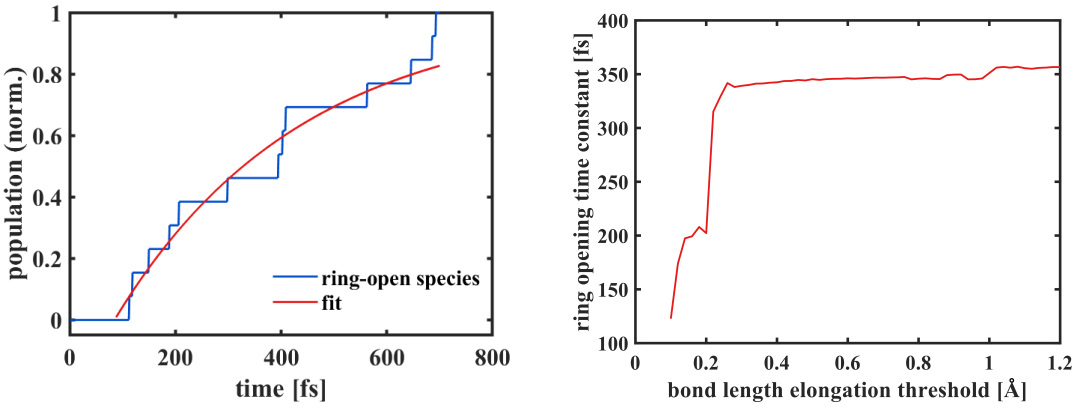

(a) (b)

Fig. S8: Formation of ring-open isomers in the excited state dynamics simulations based on analysing the C-O distances in trajectories leading to MC. (a) Normalised population of ring-open species obtained by setting a C-O distance elongation threshold of 1Å, fitted with a monoexponential function with a time constant of 350 fs and starting at 88 fs. (b) Obtained time constants for different threshold values. Below 0.3 Å, the analysis becomes affected by fluctuations of the bond length around the equilibrium value.

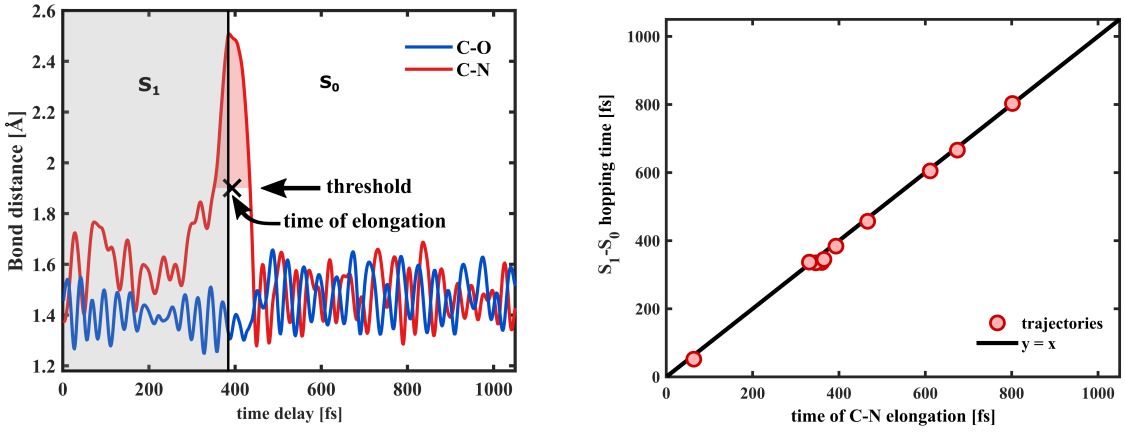

(a) (b)

Fig. S9: Relaxation to the reactant ground state via C-N bond elongation. (a) Representative example trajectory. The vertical line marks hopping from S1 to S0 for the shown trajectory. The time of C-N elongation is obtained by taking the mean of the delay times during which the C-N bond is elongated above the half-maximum value. (b) Correlation between S1 to S0 hopping and C-N elongation for all internal conversion trajectories, as shown in the main manuscript.

3 Steady-state absorption measurements

The complete set of absorption spectra of SNP in the three solvents is presented in Fig S10 and Fig S11. The MC spectra consist of three identifiable peaks. The positions of these peaks are given in Table S5. The table is arranged such that the highest polarity solvent is at the top and the least polar at the bottom. According to the table, a red-shift of the peak position takes place when going from nonpolar solvent (hexane) to a polar aprotic (acetonitrile) and polar protic solvent (ethanol). The shifts are likely a result of stabilisation induced by the solvent of either the ground or excited state. The ground state of merocyanine formed from a dinitro-substituted SNP has been reported to have zwitterionic character[5], which would imply that polar media stabilise the energy of the ground state relative to the excited state and thus, lead to an increase in the HOMO-LUMO gap which then will shift the maximum to shorter wavelengths. This is clearly not observed, which suggests that in polar media it is the excited state that is stabilised more than the ground state and that the excited state dipole moment is higher than the ground state dipole moment. The spectrum in ethanol is red-shifted even further (shift of max. $\Delta\lambda = 7$ nm with respect to acetonitrile), despite the lower polarity of the solvent compared to acetonitrile. This suggests that hydrogen bonding is responsible for the red-shift perturbing the charge distribution in MC in such a way that the excited state is further lowered in energy, though the effect is not dramatic.

Table S5: Peak positions from the steady-state spectra of MC. Peaks are numbered in descending order with respect to wavelength.

Solvent	Peak 1	Peak 2	Peak 3
Acetonitrile	565 nm	529.6 nm	492.1 nm
Ethanol	569.8 nm	536 nm	498 nm
Hexane	558.1 nm	520.8 nm	482.7 nm

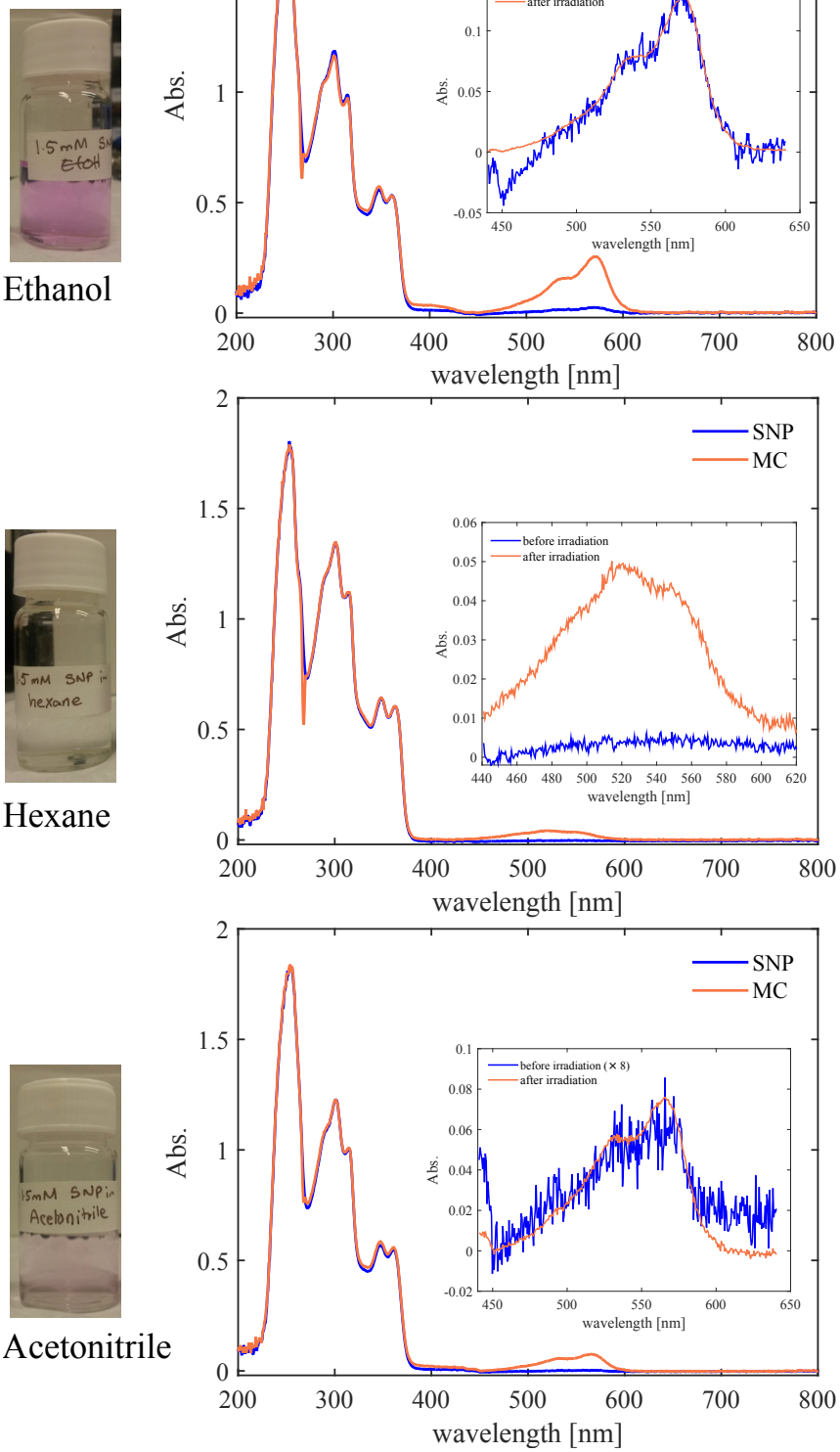

Fig. S10: Absorption spectra of SNP. The photoinduced form created is compared with the that found at thermal equilibrium (see insets). In hexane, the MC form is absent at thermal equilibrium.

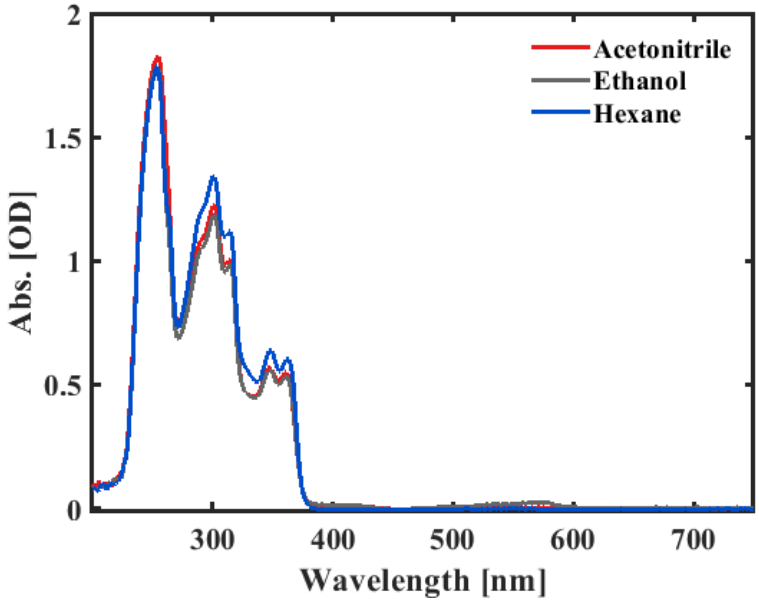

Fig. S11: Absorption spectra of the SNP solutions irradiated with a 266 nm femtosecond laser until a steady spectrum had been reached. The data is the same as in the inset of Fig 2, but without scaling and showing the whole spectral range that was measured.

4 Transient absorption spectroscopy

4.1 UV/Vis transient absorption maps

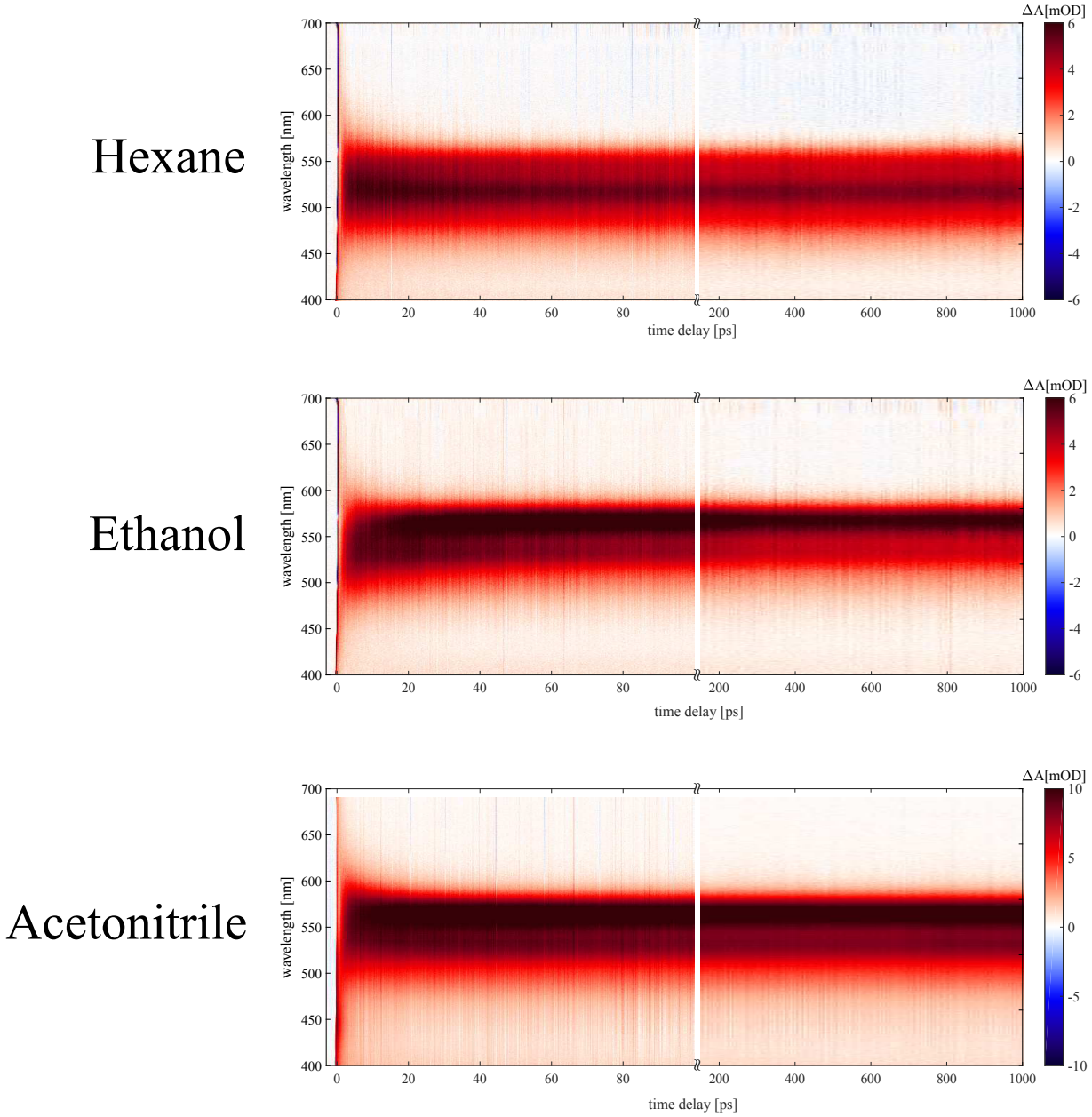

Fig. S12: UV/Vis scans up to 1 ns after excitation. The dynamics are essentially complete after approximately 50-60 ps as evidenced by the constancy of signals in visible range for all solvents.

4.2 UV/Vis transient absorption maps-False Colour

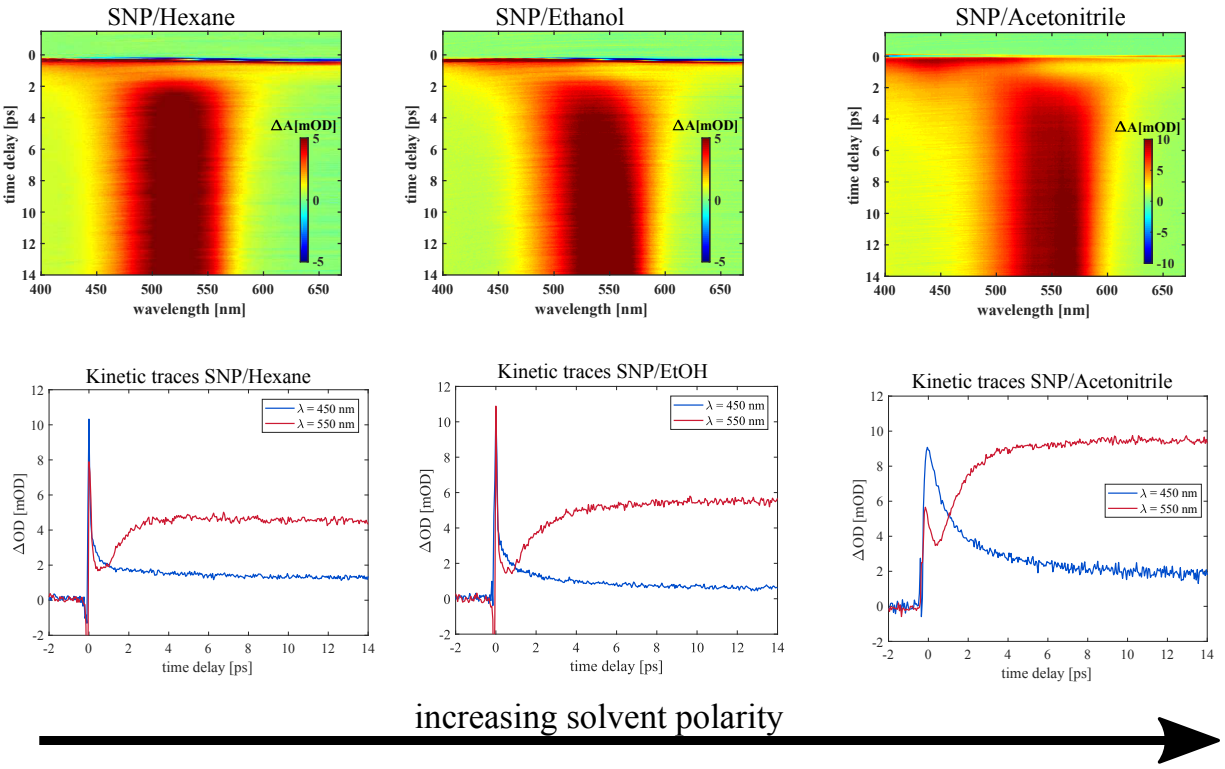

Fig. S13: UV/Vis maps of short range (0-14 ps) and kinetic traces for 2 chosen wavelengths, i.e. $\lambda = 450$ nm and 550 nm in three solvents.

4.3 Integrated TA product bands

In order to further support the assignment of the product formation time scale and eliminate possible errors from spectral shifts and narrowing, the TA spectra were integrated over the wavelength region in which the product absorbs in the respective solvents and fit with three exponential functions for time delays between 0.2 and 13 ps. For the initial fast decay observed in all three cases, a time constant of around 300 fs was found varying for the different solvents between 260 and 350 fs. The following rise was fitted with an exponential function with a time constant of 1.1, 1.0 and 0.9 fs for acetonitrile, ethanol and hexane, respectively. The third exponential function converged to a constant in case of ethanol and acetonitrile and to a long-lived decay in case of hexane, with a time constant of 130 ps, which is an order of magnitude longer than the time range. These findings further support the claim that the chemical reaction takes places with a time constant of 1 ps and spectral dynamics on a longer time scale are related to product equilibration.

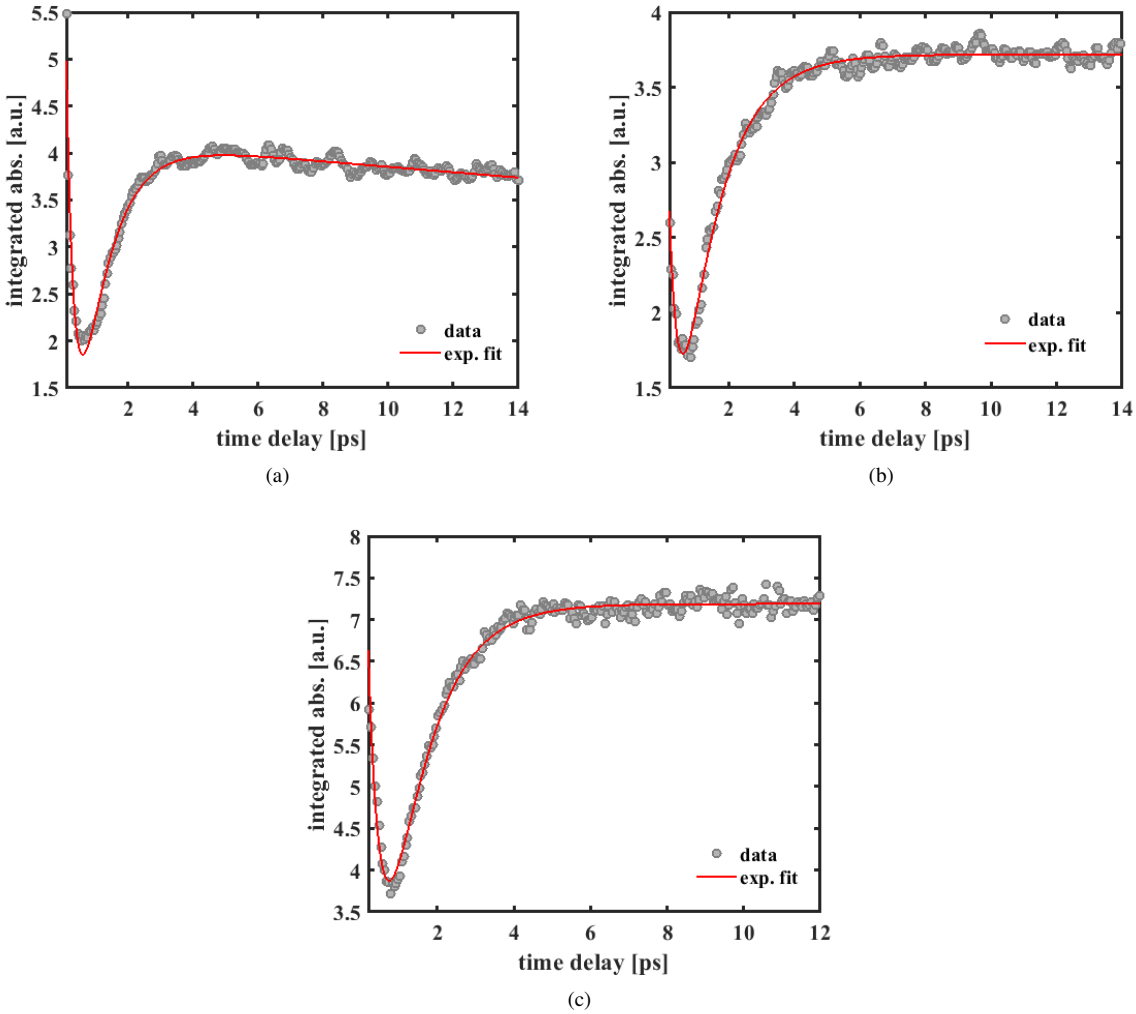

Fig. S14: TA spectra integrated over the region of product absorption between 450-470 and 570-605 nm depending on the solvent (a: Hexane, b: Ethanol, c: Acetonitrile). The data were fit with a sum of three exponential functions.

4.4 UV/UV transient absorption maps

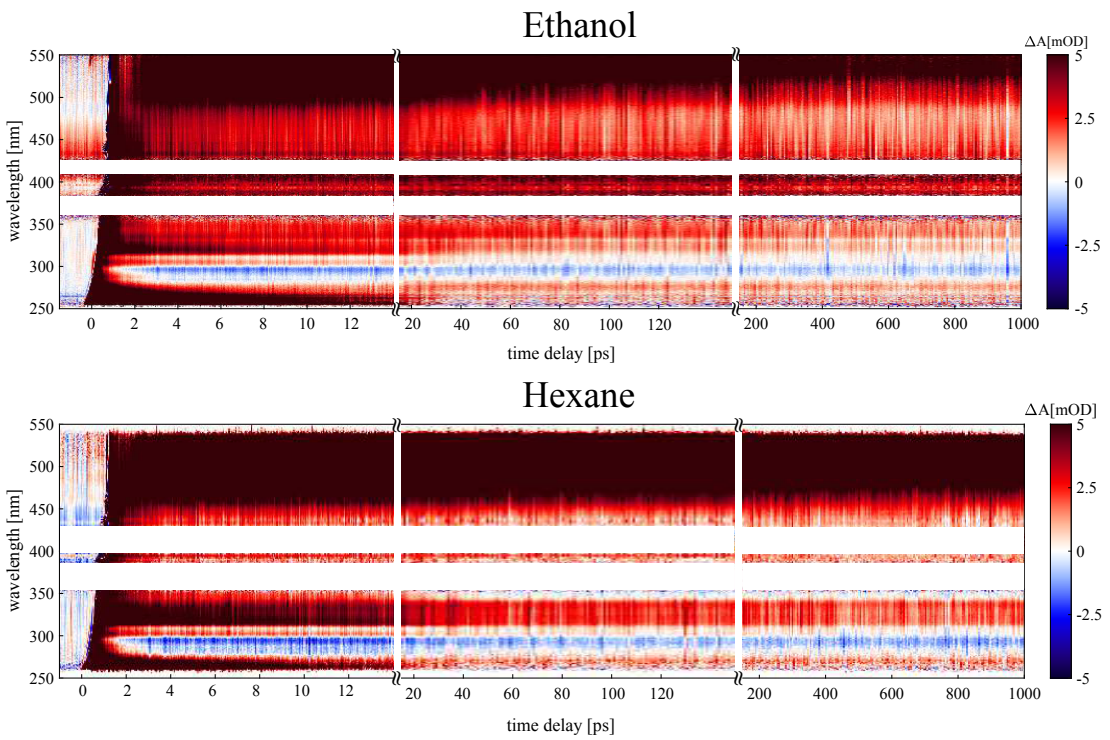

Fig. S15: UV/UV scans. Three different step sizes were employed: 50 fs (left), 1 ps (middle) and 5 ps (right). The slight decrease in signal intensity and increase in noise level is due to drops in laser power owing to mid-term drifts and less averaging going from left to right, respectively. One complete scan took approximately 40 minutes. Note, the data were not normalised to the pump laser power.

4.5 Fluence dependence

The intensity of the pump pulse was varied and transient absorption spectra were recorded in order to measure the fluence dependence. The plots from these measurements are shown in Fig S16. The response was found to be linear up to 5 mJ cm^{-2}.

4.6 Acquisition scheme

For UV/UV measurements, the pump beam scatter became an issue as this unwanted signal appeared before the time-zero was reached, i.e. at negative time delays. To circumvent this, we adopted the dual-chopping scheme[6]that allowed us to cancel the pump scatter signal. To achieve this, two mechanical choppers were placed, one in the pump line and the other in the probe line. The chopper in the pump line was triggered with the signal from main laser clock —a 1 kHz TTL, and was set to modulate the frequency to a one half. A photodiode was placed in the beam line after the mechanical chopper in order to record the shots at which the pump was ON. Furthermore, the chopped signal at 500 Hz, measured by the photodiode, was used to trigger the mechanical chopper in the probe arm, set to output 1/2 of the input frequency. To verify that this generated the correct pulse ordering, a photodiode was placed after the probe line as well and the two choppers were run and the chopped signals were measured simultaneously. The recorded signal are displayed in Fig S17. As the figure shows, the sequence that is produced is:

1. Pump and Probe ON
2. Probe only ON
3. Pump only ON
4. Pump and Probe both OFF

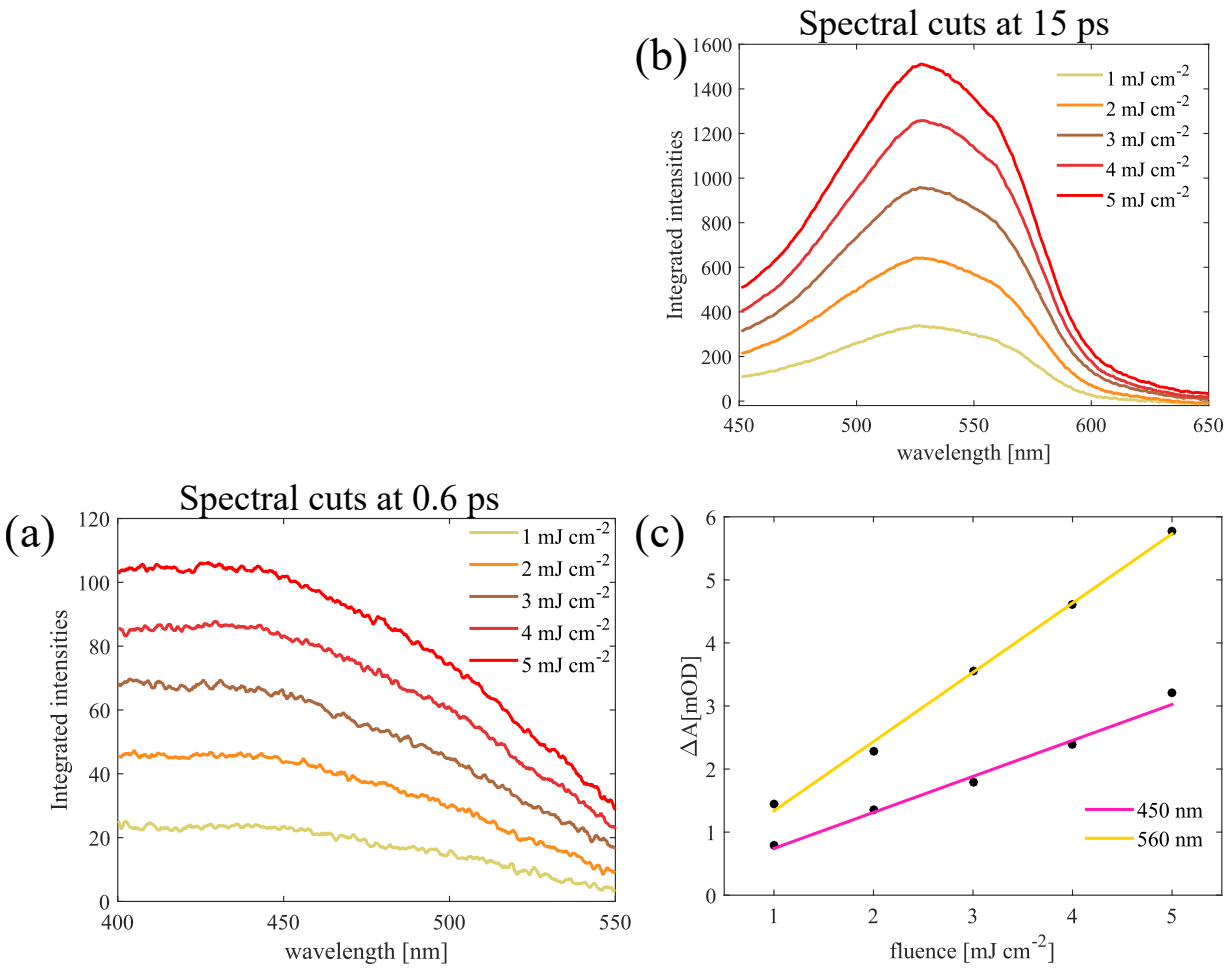

Fig. S16: Spectral plots covering range 400-550 nm in (a) and 450-650 nm in (b) are provided for different fluences. A plot of the maximum change in optical density as a function of fluence at 450 nm and 560 nm is also presented in (c). A linear fit is also shown and demonstrates the linearity of the signal at the chosen fluence at which the experiments were performed.

Pulse number 1 and 2 carried the signals from excited and unexcited sample, respectively. Pulse number 3 contained the pump beam background whereas Pulse 4 measured the detector (dark) background. Fig S18 compares the two cases, when dual chopping was implemented (Fig S18a) and the when it was not (Fig S18b).

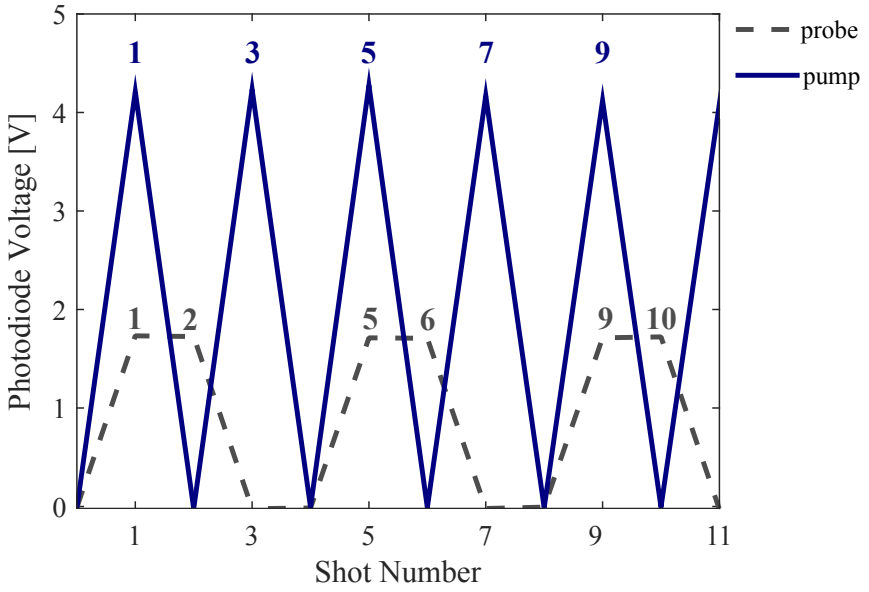

Fig. S17: The voltage measured by a photodiode placed in the probe line (shown in grey) and pump line (shown in blue).The shots are numbered according to the sequence that they appear in.

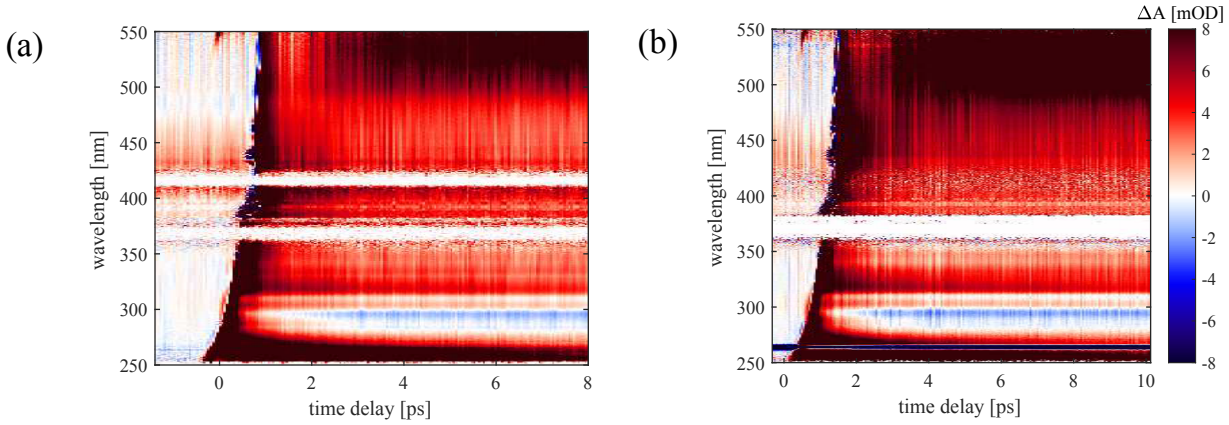

Fig. S18: Transient absorption maps using 266 nm pump measured implementing the dual-chopping scheme (a) and in the conventional pump ON-pump OFF manner (b).

5 Global analyses

All transient absorption (TA) data were treated with a global fit routine developed in house. In each case, the minimum required number of components was found by comparison regarding the fit quality, i.e. fit residual and phenomenological representation of the data. For the visible data shown here, four components were required for an accurate fit. Figures S19 - S21 show the data, DAS, global fit and residual for the visible TA performed in hexane, ethanol and acetonitrile, respectively. The time window for the analysis was 0.3-14 ps. The interpretation of the DAS and the associated decay times can be found in the main manuscript.

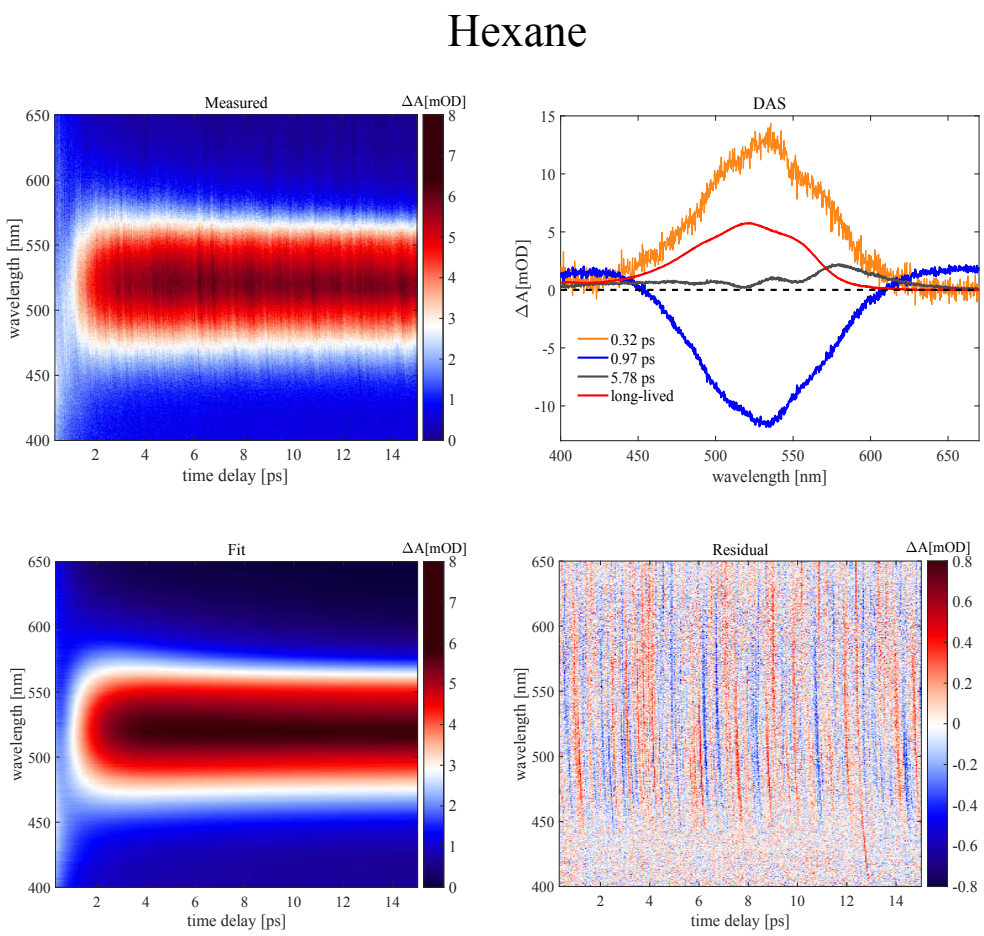

Fig. S19: Global analysis of the TA data in the visible range of SNP in n-hexane. Shown are the measured data, the DAS, the resulting fit and the residual.

Ethanol

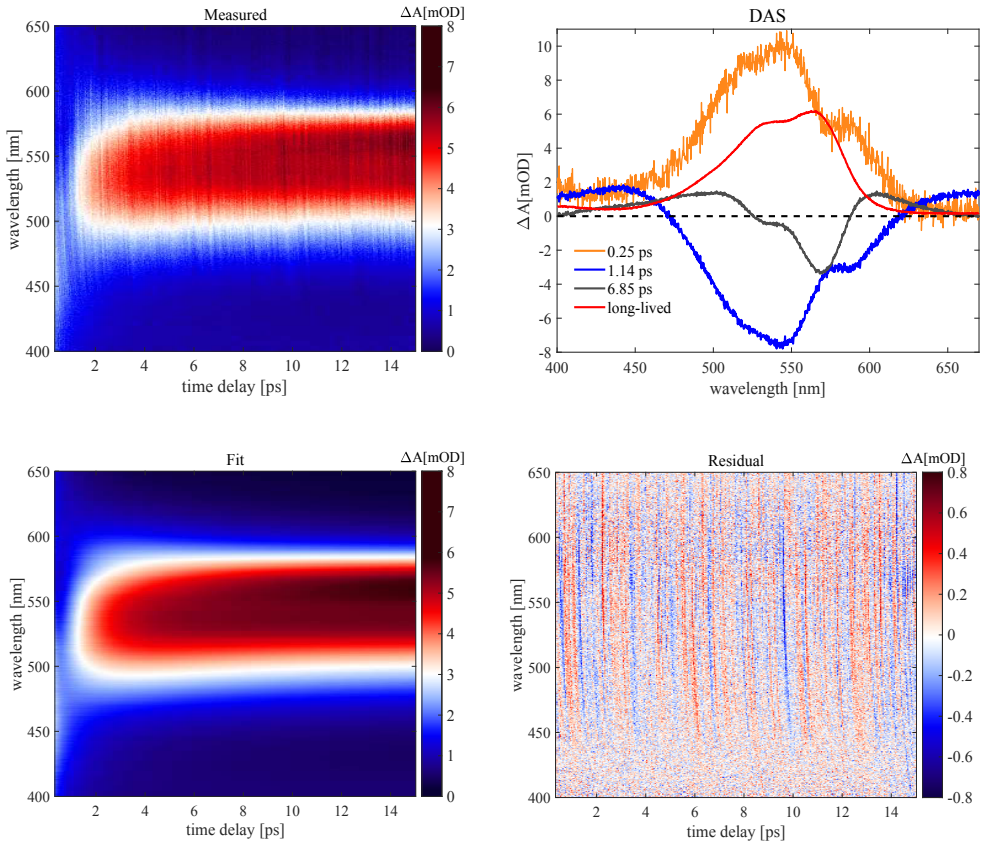

Fig. S20: Global analysis of the TA data in the visible range of SNP in ethanol. Shown are the measured data, the DAS, the resulting fit and the residual.

Acetonitrile

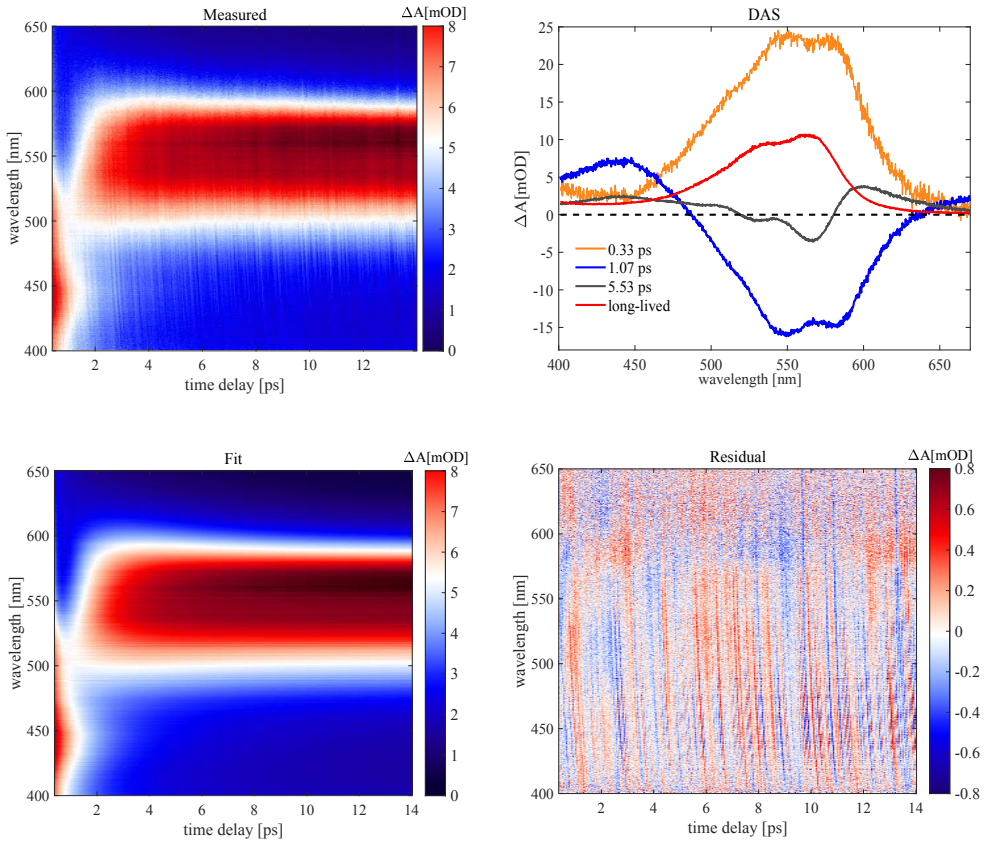

Fig. S21: Global analysis of the TA data in the visible range of SNP in acetonitrile. Shown are the measured data, the DAS, the resulting fit and the residual.

6 Gaussian modeling

6.1 Model comparison

In order to describe the product relaxation dynamics, the transient absorption data recorded in the visible were treated with a dynamic Gaussian line shape analysis using nonlinear least-squares fitting. For each time point, the TA spectra were fitted with the following sum of Gaussians:

$$\sum_{i}^{N} A_i e^{-\frac{(\bar{\nu}-b_i)^2}{2\sigma_i^2}} + C \tag{S6.1.1}$$

where *N* is the number of Gaussian functions, $\bar{\nu}$ is the frequency in wavenumbers, (cm^{-1}), A_i, b_i and σ_i are the amplitude, central frequency and width of the *i*-th Gaussian (i going from lowest transition energy to highest), and C denotes an offset that accounts for probe fluctuations. All fits were done starting with the spectrum at the latest time delay (99 ps), at which the spectral shapes were identical with the respective steady-state spectra, and taking the resulting parameters as initial guesses for the preceding time point. This was repeated down to a time delay of 9 ps, at which the spectra became too diffuse to yield accurate fits.
Fitting the spectra was tested using three and four Gaussians with and without the offset. In addition, the physical picture of a vibrational progression being the origin of the spectral fine structure was introduced and tested by imposing the following constraints on the parameters. Approximating the excited state electronic potential as harmonic, an equal spacing δ between the peaks was introduced as fit parameter instead of independent values of b_i:

$$b_i = b_1 + (i-1)\cdot\delta \tag{S6.1.2}$$

Assuming that the peak broadening is governed by fluctuations of the potential due to the environment, two different correlations between the peak widths were tested:

$$\sigma_i = i \cdot \sigma_1. \tag{S6.1.3}$$

$$\sigma_i = \left(i - \frac{1}{2}\right) \cdot \sigma_1. \tag{S6.1.4}$$

The following combinations of the discussed constraints were tested to evaluate their suitability, all with and without the additional offset parameter:

1. Equal spacing and constrained widths
2. Equal spacing and independent widths
3. Independent spacing and constrained widths
4. Independent spacing and independent widths

The evaluation was carried out regarding the residual of the fit as well as the stability of the fitting parameters within the analysed time window.

It was found that combination 1 with the offset gave the best fits for all solvents. The best results for acetonitrile and hexane were achieved with four Gaussians, while in ethanol the amplitude of the fourth Gaussian turned out to be very close to the noise level leading to a decrease in stability. For this reason, additional fits with the same model but only three Gaussians were carried out and analysed for the ethanol solution.
Within model 1, a linear correlation between peak widths (S6.1.3) led to the best residuals and stabilities. It should be pointed out that a Gaussian fit represents only a coarse approximation and the more accurate modelling would be using Voigt profiles where a Lorentzian curve, whose width corresponds to the finite life time, is convoluted with a Gaussian that accounts for inhomogeneous broadening. The systematic error of using Gaussians is also visible in the residuals (see Figs S22-S24), assuming positive values at the centres of the respective functions (shifted slightly because the curves overlap) and negative residuals between them, which matches the difference in shape between a Gaussian curve and a Voigt profile. However, line shape fits with Voigt profiles were unstable over time because of the additional fit parameter for each curve. For this reason, quantitative statements on the nature of the potential and the line broadening cannot be discussed based on the model itself. The key insights from being able to apply this simplified model are an indication that the fine structure is most likely due to a vibrational progression, a correlation between the peak widths and the time scale of peak narrowing as a signature of product relaxation, which is discussed in the following section.

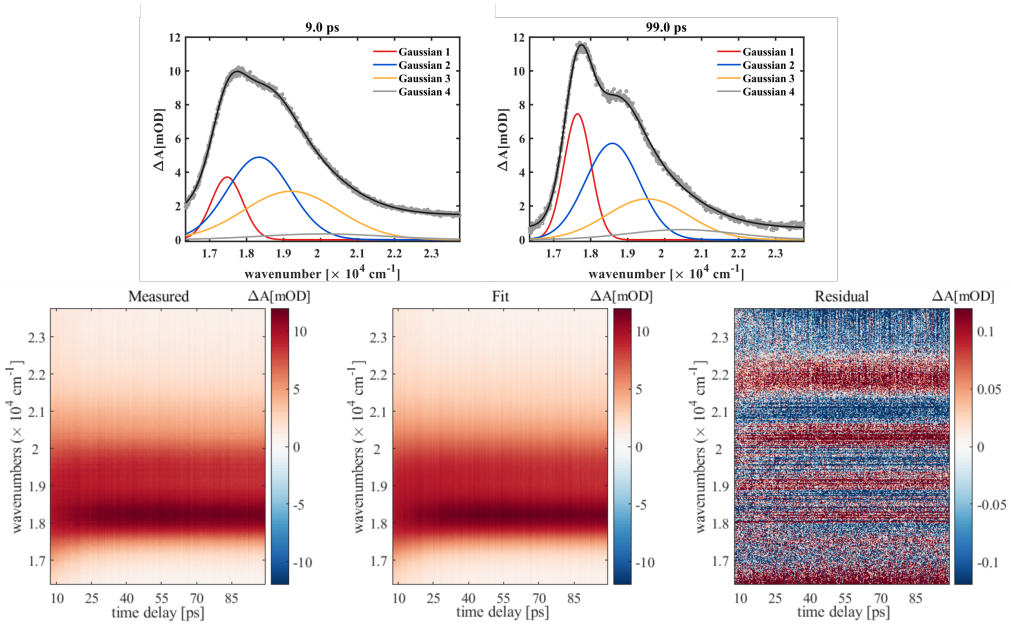

Fig. S22: Dynamic Gaussian line shape analysis of SNP in acetonitrile, fitted with four Gaussians, model 1.

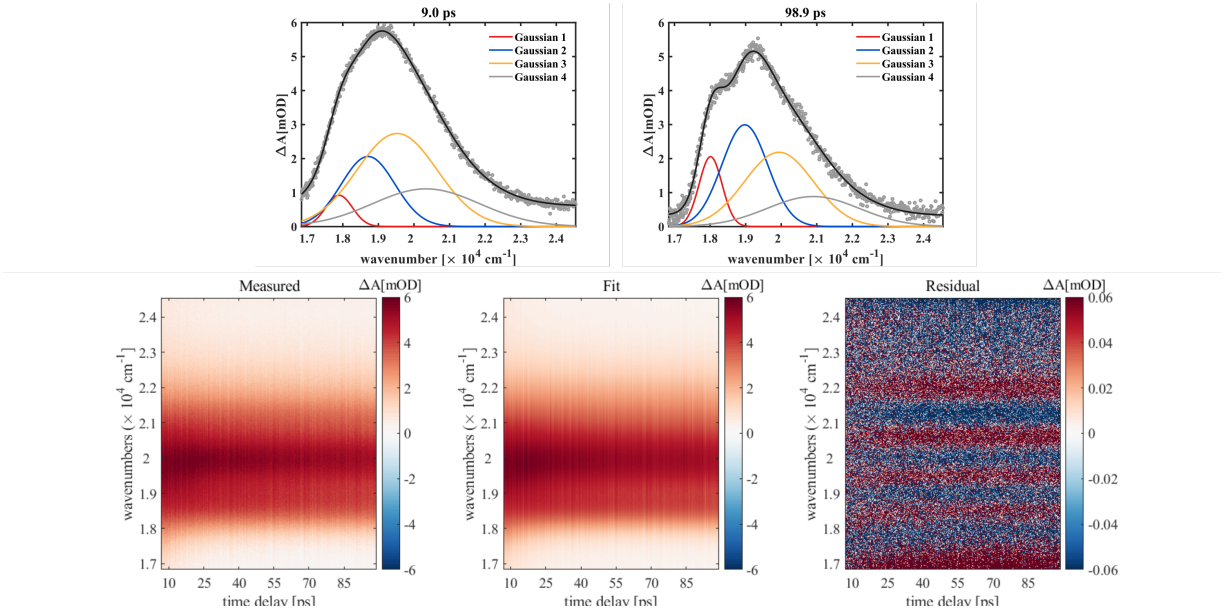

Fig. S23: Dynamic Gaussian line shape analysis of SNP in hexane, fitted with four Gaussians, model 1.

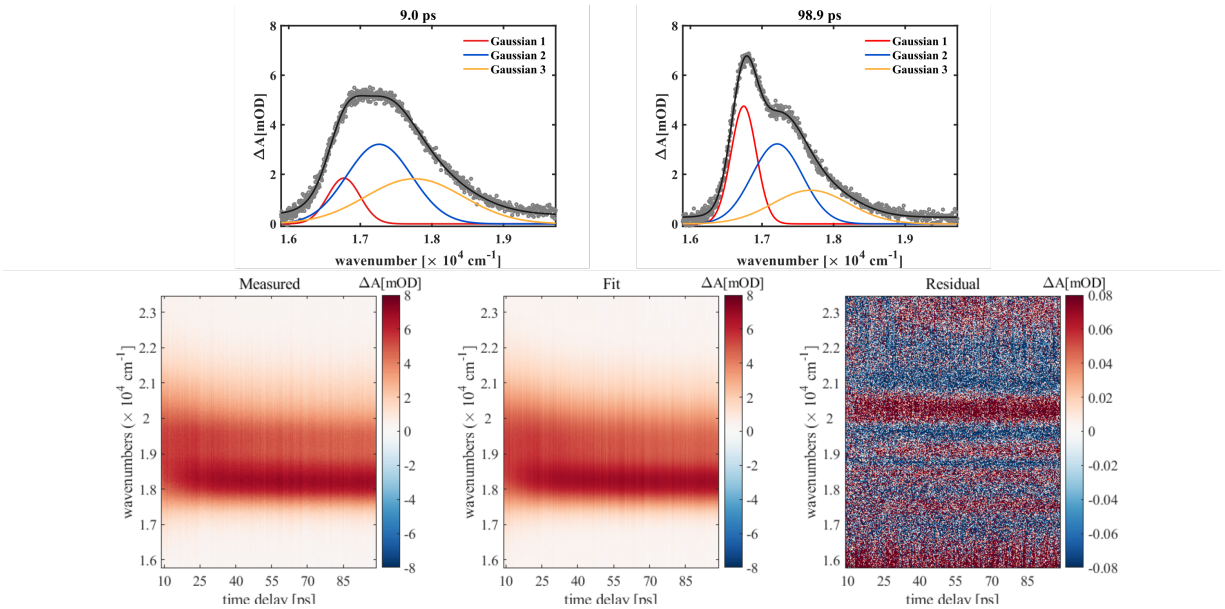

Fig. S24: Dynamic Gaussian line shape analysis of SNP in ethanol, fitted with three Gaussians, model 1.

6.2 Relaxation dynamics analysis

The Gaussian peak positions, widths and areas from the selected models for each solvent were retrieved and their temporal evolution between 9 and 99 ps was fitted using exponential functions. The widths were fitted with mono-exponential functions including an offset for their equilibrium value. The same procedure was applied to the two parameters that define the peak positions (see equation S6.1.2), i.e. the overall spectral position, which is reflected by the position b_1 of the lowest energy peak, and the equal spacing δ between the peaks. The peak areas were fitted in general with a sum of two exponential functions, but in some cases the second term adopted very long decay constants in comparison to the measured time range, which corresponds to an effectively monoexponential behaviour.

The retrieved exponential parameters for peak positions and widths are collated in Table S6. The dynamics are very similar for acetonitrile and hexane, exhibiting an overall blue-shift of the transition energies with time constants of 13 ps in both cases, which exactly matches the decay times of the respective FWHM values. The peak spacing increases over time in both solvents with slightly different time constants (21 ps for acetonitrile and 16 ps for hexane). While the FWHM dynamics are fairly similar in ethanol (11 ps decay in case of four and 14 ps in case of three Gaussians), the positions reflect the red-shift observed in the measurement. When using four Gaussians, the time constant of the red-shift proved to depend significantly on the model ranging between 20 and 70 ps, unlike the FWHM values, which varied only between 11 and 14 ps. This instability is likely due to the mentioned uncertainty introduced by the fourth Gaussian. Thus, more reliable information can be obtained when using three Gaussians. The equilibrium parameters of the first three Gaussians are identical in both cases, which is in accordance with the fourth Gaussian being very small in amplitude and negligible when using a linear offset. In case of three Gaussians, a time constant of 49 ps is obtained for the red-shift, while the spacing decreases with a time constant of 35 ps. Both results are in contrast to the findings in the other two solvents.

Table S7 shows the fitting results for the peak areas. Besides similar rise times of the lowest energy peak between 12.3 and 17.5 ps, no clear similarities or differences between the different solvents can be found. In the context of a vibrational progression, the areas correspond to transition probabilities, which depend on the vibrational wave-function overlaps on the electronic ground and excited state potential energy surfaces (Franck-Condon rule). The temporal development of the peak areas allows thus no conclusions beyond a descriptive level. However, these observations encourage further investigations of the dynamic vibronic structure of the ground and excited state.

Table S6: Temporal development of Gaussian positions and FWHM values. For each solvent, the monoexponential decay times τ of the respective parameters distinguishing between exponential rise (r) and decay (d) are given as well as the equilibrium values (eq. val.) averaged over the last 2 ps.

	Acetonitrile		Hexane		Ethanol (4 Gaussians)		Ethanol (3 Gaussians)	
	τ [ps]	eq. val. [cm^{-1}]	τ [ps]	eq. val. [cm^{-1}]	τ [ps]	eq. val. [cm^{-1}]	τ [ps]	eq. val. [cm^{-1}]
Position	13 (r)	$17.7 \cdot 10^3$ $18.6 \cdot 10^3$ $19.6 \cdot 10^3$ $20.6 \cdot 10^3$	13 (r)	$18.0 \cdot 10^3$ $19.0 \cdot 10^3$ $19.9 \cdot 10^3$ $20.9 \cdot 10^3$	20 (d)	$17.5 \cdot 10^3$ $18.4 \cdot 10^3$ $19.4 \cdot 10^3$ $20.4 \cdot 10^3$	49 (d)	$17.5 \cdot 10^3$ $18.4 \cdot 10^3$ $19.4 \cdot 10^3$
Spacing	21 (r)	$9.8 \cdot 10^2$	16 (r)	$9.6 \cdot 10^2$	const.	$9.2 \cdot 10^2$	35 (d)	$9.2 \cdot 10^2$
FWHM	13 (d)	859 $1.72 \cdot 10^3$ $2.58 \cdot 10^3$ $3.43 \cdot 10^3$	13 (d)	766 $1.53 \cdot 10^3$ $2.30 \cdot 10^3$ $3.07 \cdot 10^3$	11 (d)	828 $1.66 \cdot 10^3$ $2.49 \cdot 10^3$ $3.31 \cdot 10^3$	14 (d)	828 $1.66 \cdot 10^3$ $2.49 \cdot 10^3$

Table S7: Exponential fits of Gaussian areas using biexponential functions in case of the fits using four Gaussians and a single exponential with an offset in case of the ethanol fit with three Gaussians. In addition to the time constants the exponential amplitudes A are given for the former case and the offset for the latter.

	Acetonitrile		Hexane		Ethanol (4 Gaussians)		Ethanol (3 Gaussians)	
	τ [ps]	A [cm^{-1}]	τ [ps]	A [cm^{-1}]	τ [ps]	A [cm^{-1}]	τ [ps]	offset [cm^{-1}]
Area 1	17.5 (r) $1.04{\cdot}10^3$	$-5.91\cdot10^3$ $7.65{\cdot}10^3$	12.3 (r) 837 (d)	$-1.77\cdot10^3$ $1.83{\cdot}10^3$	14.0 (r) $6.37{\cdot}10^3$	$-3.90\cdot10^3$ $4.29{\cdot}10^3$	12(r)	$4.17{\cdot}10^3$
Area 2	26.2 (r) 651 (d)	$-2.50{\cdot}10^3$ $12.8\cdot10^3$	7.94 (r) $1.12{\cdot}10^3$	$-3.25\cdot10^3$ $5.26{\cdot}10^3$	9.60 (d) 760	$7.71\cdot10^3$ $7.56{\cdot}10^3$	51(d)	$5.39{\cdot}10^3$
Area 3	13.1 (d) inf (10^8)	840 $5.10\cdot10^3$	14.6 (d) $1.02{\cdot}10^3$	$3.66\cdot10^3$ $5.74{\cdot}10^3$	(3.64 (r)) 128 (d)	$-20.0\cdot10^3$ $3.30{\cdot}10^3$	32(d)	$3.6{\cdot}10^3$
Area 4	23.5 (r) 646 (d)	$-2.71\cdot10^3$ $3.88\cdot10^3$	21.7 (d) $2.64\cdot10^3$	747 $2.83{\cdot}10^3$	25.6 (d) inf (10^7)	$2.01\cdot10^3$ $2.18{\cdot}10^3$		

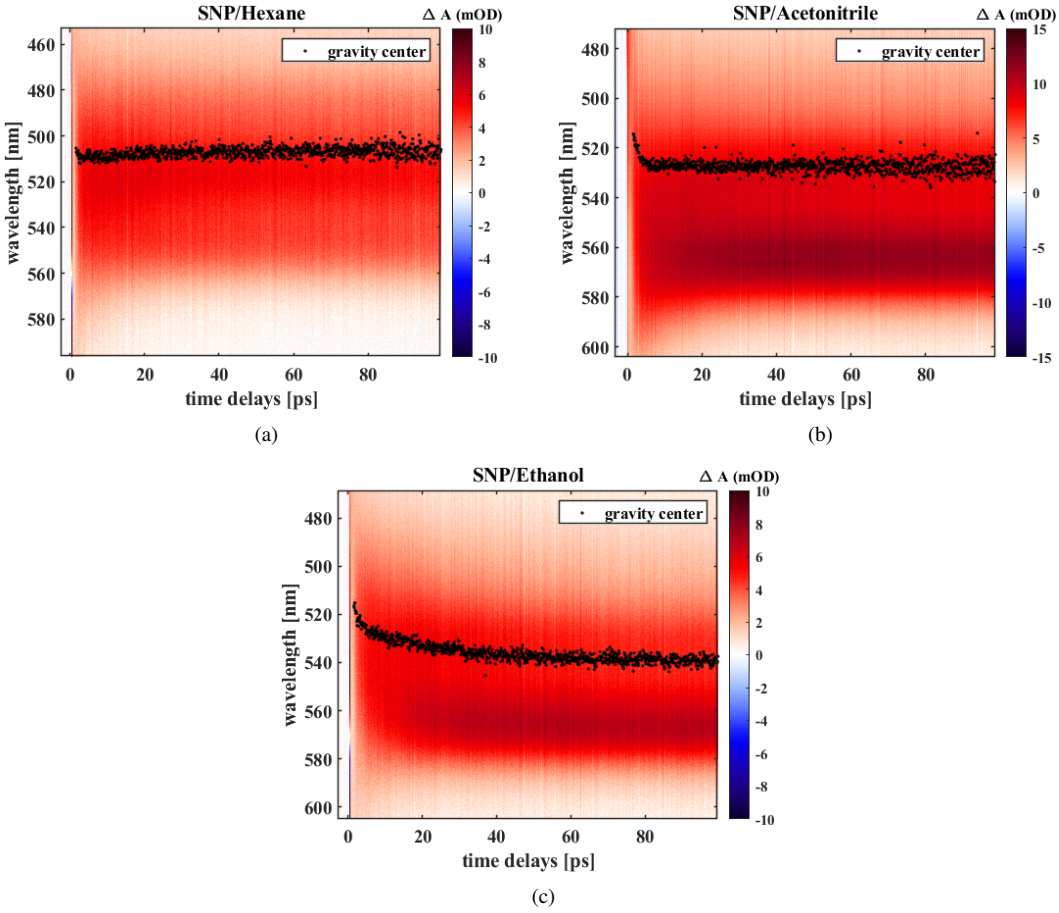

Fig. S25: Centre of gravity plots for the transient absorption data in the visible of SNP for all three solvents.

7 Centre of gravity analysis

In addition to the dynamic line shape analysis, evolution of the spectral centre of gravity was analysed. This was motivated by the fact that the line shape analysis did not lead to stable results for time delays earlier than 9 ps, as mentioned previously. The result of this analysis is shown for all three solvents in Fig S25. It reflects the observation that the initial red-shift of the spectra is completed within about 3 ps. Furthermore, the red-shift of the transition energies on a longer time scale observed in ethanol also affects the centre of gravity. The blue-shift in case of hexane and acetonitrile described by the line shape analysis is less obvious in terms of the centre of gravity, effectively disappearing in acetonitrile. This can be explained by the increase in areas of the first peak (lowest transition energy), which causes the centre of gravity to red-shift, while the transition energies blue-shift, effectively cancelling out. This underlines further the usefulness of the applied dynamic line shape analysis, where these two effects can be distinguished.

References

[1] M. Frisch, G. Trucks, H. Schlegel, G. Scuseria, M. Robb, J. Cheeseman, G. Scalmani, V. Barone, B. Mennucci, G. Petersson *et al.*, *Gaussian 09, revision D. 01*, 2009.

[2] T. Yanai, D. P. Tew and N. C. Handy, *Chemical Physics Letters*, 2004, **393**, 51–57.

[3] R. Dsouza, X. Cheng, Z. Li, R. J. D. Miller and M. A. Kochman, *The Journal of Physical Chemistry A*, 2018, **122**, 9688–9700.

[4] T. Version, *Turbomole is a development of University of Karlsruhe and Forschungszentrum Karlsruhe*, 1989, **2007**, year.

[5] W. Tian and J. Tian, *Dyes and Pigments*, 2014, **105**, 66–74.

[6] V. I. Prokhorenko, A. Halpin, P. J. M. Johnson, R. J. D. Miller and L. S. Brown, *The Journal of Chemical Physics*, 2011, **134**, 085105.